

# **Robust field re-entrant superconductivity in ferromagnetic infinite-layer rare-earth nickelates**

Mingwei Yang<sup>1,11</sup>, Jiayin Tang<sup>1,11</sup>, Xianfeng Wu<sup>2,11</sup>, Heng Wang<sup>2,3\*</sup>, Wenjing Xu<sup>1,4</sup>, Haoliang Huang<sup>2,3</sup>, Zhicheng Pei<sup>1</sup>, Wenjie Meng<sup>5</sup>, Guangli Kuang<sup>5</sup>, Jinfeng Xu<sup>6</sup>, Sixia Hu<sup>2</sup>, Chuanying Xi<sup>5</sup>, Li Pi<sup>5,6</sup>, Qingyou Lu<sup>5,7,8</sup>, Ziqiang Wang<sup>9</sup>, Qikun Xue<sup>2,3,10</sup>, Zhuoyu Chen<sup>2,3\*</sup>, Danfeng Li<sup>1,4\*</sup>

<sup>1</sup>*Department of Physics, City University of Hong Kong, Kowloon, Hong Kong SAR, China.*

<sup>2</sup>*Department of Physics, State Key Laboratory of Quantum Functional Materials, and Guangdong Basic Research Center of Excellence for Quantum Science, Southern University of Science and Technology, Shenzhen 518055, China.*

<sup>3</sup>*Quantum Science Center of Guangdong-Hong Kong-Macao Greater Bay Area, Shenzhen 518045, China.*

<sup>4</sup>*Shenzhen Research Institute of City University of Hong Kong, Shenzhen 518057, China.*

<sup>5</sup>*Anhui Key Laboratory of Low-Energy Quantum Materials and Devices, High Magnetic Field Laboratory, HFIPS, Chinese Academy of Sciences, Hefei 230031, China.*

<sup>6</sup>*Institute of High Energy Physics, Chinese Academy of Sciences, Beijing 100049, China.*

<sup>7</sup>*Hefei National Research Center for Physics Sciences at the Microscale, University of Science and Technology of China; Hefei 230026, China.*

<sup>8</sup>*Hefei National Laboratory, University of Science and Technology of China, Hefei 230026, China.*

<sup>9</sup>*Department of Physics, Boston College, Chestnut Hill, MA, USA.*

<sup>10</sup>*Department of Physics, Tsinghua University, Beijing 100084, China.*

<sup>11</sup>*These authors contributed equally: Mingwei Yang, Jiayin Tang, Xianfeng Wu.*

*\*Corresponding author: [wangheng@quantumsc.cn](mailto:wangheng@quantumsc.cn), [chenzhuoyu@sustech.edu.cn](mailto:chenzhuoyu@sustech.edu.cn), [danfeng.li@cityu.edu.hk](mailto:danfeng.li@cityu.edu.hk).*

## Abstract

Superconductivity and ferromagnetism are naturally competing, while their interplay can give rise to exotic quantum phases, such as triplet pairing, exemplified by heavy-fermion compounds like  $\text{UTe}_2$ , where magnetic fluctuations stabilise multiple superconducting states. However, such phenomena have remained elusive in high-temperature superconductors. Here we report the discovery of robust field-induced re-entrant superconductivity in heavily Eu-doped infinite-layer nickelate  $\text{Sm}_{0.95-x}\text{Ca}_{0.05}\text{Eu}_x\text{NiO}_2$ . In the heavily over-doped regime, we observe a remarkable superconducting state that emerges under high magnetic fields ( $> 6$  Tesla) after the initial suppression of zero-field superconductivity. Both zero-resistance transport and Meissner diamagnetic effect confirm the superconducting nature of this high-field phase, which persists up to at least 45 Tesla. This re-entrant behaviour is featured by the coexistence of ferromagnetism and superconductivity on distinct sublattices—magnetic  $\text{Eu}^{2+}$  ions and the Ni-O planes, respectively. Such an exotic state may arise from the compensation between external and internal exchange fields (Jaccarino-Peter effect) combined with magnetic fluctuation-enhanced pairing near quantum criticality. Our findings establish infinite-layer nickelates as a unique platform for high-temperature ferromagnetic superconductivity, opening new avenues for discovering and manipulating unconventional quantum phases in strongly correlated materials.

## Introduction

The interplay between magnetism and superconductivity can give rise to some of the most exotic quantum phases in condensed matter physics, such as high-temperature superconductivity<sup>1–3</sup>, chiral superconductivity<sup>4,5</sup> and topological superconductivity<sup>6,7</sup>. While these phenomena are traditionally antagonistic—magnetism typically destroys Cooper pairs through orbital and paramagnetic effects—certain rare circumstances allow their coexistence and even mutual enhancement<sup>8,9</sup>. Preliminary experimental evidence for such delicate balance has been prominently observed in heavy-fermion compounds, where magnetic fluctuations near quantum critical points may mediate unconventional pairing mechanisms, leading to phenomena such as field-induced and re-entrant superconductivity<sup>10–23</sup>. The paradigmatic examples include uranium-based superconductors like  $\text{UTe}_2$ <sup>15–18</sup>,  $\text{UGe}_2$ <sup>19,20</sup>, and  $\text{URhGe}$ <sup>21–23</sup>, where spin-triplet superconductivity emerges in the presence of strong magnetic correlations<sup>15–23</sup>. In  $\text{UTe}_2$ , superconductivity remarkably survives magnetic fields far beyond the conventional Pauli limit and exhibits multiple superconducting phases that can be accessed through field tuning<sup>15–18</sup>. Similarly,  $\text{UGe}_2$  displays superconductivity under pressure in proximity to its ferromagnetic-like state<sup>19,20</sup>, while  $\text{URhGe}$  shows field-induced re-entrant superconductivity<sup>21–23</sup>. These phenomena arise from sophisticated mechanisms, including the Jaccarino-Peter effect<sup>8,9</sup> and magnetic fluctuation-enhanced pairing near quantum phase transitions<sup>15–23</sup>, and predominantly observed at extremely low temperatures.

The cuprate superconductors are a representative system for intertwined superconducting and antiferromagnetic orders<sup>1</sup>, yet the inclusion of ferromagnetic order and the demonstration of the field-stabilised superconducting phases have been elusive. This absence has limited our understanding of whether magnetic fluctuation-mediated mechanisms can operate in higher- $T_c$  systems and has left open fundamental questions about the universality of such exotic superconducting phases.

The recently discovered infinite-layer nickelates have emerged as a transformative new platform that potentially bridges high-temperature superconductivity and ferromagnetic instabilities<sup>24–33</sup>. These materials, with transition temperatures reaching up to  $\sim 35\text{ K}$ <sup>32,33</sup>, are highly similar to cuprates in electronic structures, while retaining important differences, particularly the role of rare-earth elements<sup>34–38</sup>. Recent Eu doping in  $\text{NdNiO}_2$  opens unprecedented possibilities for introducing ferromagnetism while maintaining superconducting properties<sup>31</sup>:  $\text{Eu}^{2+}$  ions carry large magnetic moments ( $S = 7/2$ ) that may introduce substantial magnetic interactions. The question of how varying Eu doping levels affects the delicate balance between local magnetic moments and itinerant superconductivity represents a crucial unexplored territory that could reveal novel quantum phases.

In this work, we systematically investigate the phase diagram of  $\text{Sm}_{0.95-x}\text{Ca}_{0.05}\text{Eu}_x\text{NiO}_2$  across an ultrawide range of Eu concentrations, revealing the emergence of ferromagnetic order that coexists with superconductivity in the heavily doped regime. Most remarkably, we discover robust field-induced re-entrant superconductivity persisting to at least 45 Tesla. Through comprehensive transport, magnetic, and structural characterisation, we demonstrate that this exotic behaviour arises from the interplay between magnetic  $\text{Eu}^{2+}$  sublattices and superconducting Ni-O planes. These findings establish infinite-layer nickelates as an

unprecedented materials platform that brings together concepts from high-temperature and heavy-fermion superconductivity, opening entirely new avenues for engineering exotic quantum phases in strongly correlated materials.

## Results

Multiple sets of  $\text{SCE}_x$  samples with changing Eu concentration were prepared (for sample growth, see Methods). X-ray diffraction data for representative precursor perovskite and product infinite-layer phases are shown in Extended Data Fig. 1 in the Supplementary Information, which indicates overall good crystallinity. The temperature-dependent resistivity,  $\rho(T)$ , normalised by its room-temperature value  $\rho(300 \text{ K})$ , for one set of samples with varying  $x$  is plotted in Fig. 1a. An interesting observation can be immediately made for  $x = 0$  and  $x < 0.10$ :  $\text{SCE}_x$  samples show an insulating behaviour with increasing  $\rho(T)$  as temperature decreases. This is in direct contrast to the metallic behaviour as the precursor to a low-temperature weakly insulating state observed across other doped infinite layer nickelate systems<sup>25,26,39</sup>, despite a 5% Ca doping introduced even for  $x = 0$  in  $\text{SCE}_x$ .

As  $x$  increases, a metallic behaviour with a slight resistivity upturn at low temperatures accompanies the occurrence of the superconducting transition, first manifested as a downturn in resistivity ( $x = 0.1$ ), before unveiling full transitions to a zero-resistance ground state with the superconducting transition temperature  $T_c$  following a non-monotonic manner ( $x = 0.1 \sim 0.45$ ). Upon further doping,  $T_c$  vanishes, and the system becomes a metal in almost the entire temperature range, with a clear change in the slope of the  $\rho(T)$  curves. At these high doping levels ( $x > 0.45$ ), a mild resistivity upturn is usually observed, indicative of disorder. These phenomena are consistent with a modulation of the ground state through the carrier doping effect, as evidenced by a pronounced peak shift toward lower energy in the Eu- $M$  edge spectra (Fig. 1b) measured by X-ray absorption spectroscopy (XAS). The evolution of the Eu- $M_5$  edge peaks is shown in the inset of Fig. 1b, featuring an increasing proportion of  $\text{Eu}^{2+}$  ions<sup>40–42</sup>, effectively ‘hole-doping’ the system.

A colour map is shown in Fig. 1c, made of a contour plot of the  $x$ -dependent normalised  $\rho(T)$  data ( $x = 0.10 \sim 0.6$ ) for  $\text{SCE}_x$ , showcasing a robust ‘dome’-shape superconducting regime that is the centrepiece of the superconducting phase diagram. The maximum of  $T_c$  (onset) is  $\sim 30 \text{ K}$ . The doping range in which superconductivity is present spans  $0.08 < x < 0.5$ , broader than that reported for the  $\text{Nd}_{1-x}\text{Eu}_x\text{NiO}_2$  system ( $0.15 < x < 0.4$ )<sup>31</sup>. In addition to the expanded superconducting phase diagram, we observed that the samples retain excellent phase purity even under heavy doping levels of  $x = 0.6$ , with crystallinity maintained across the entire doping regime. As demonstrated in Extended Data Fig. 2, the  $x = 0.8$  doped sample exhibits a consistent crystallinity, though it lies much beyond the superconducting dome and is not the focus of this study. This observation further corroborates that the solubility limit of Eu as a dopant significantly exceeds that of Sr or Ca, reflecting its superior compatibility with the host lattice.

To unveil the quasiparticle scattering pertaining to superconductivity in the normal state, either a linear- or quadratic- $T$  dependent function was applied to fit the  $\rho(T)$  data. The linear- $T$  dependence was mainly used for  $x$  values that are close to the optimal doping levels (on top of



the ‘dome’)<sup>1,3</sup>, where in a large temperature range  $\rho(T)$  shows a clear linear- $T$  dependent behaviour; the linear-dependence functions fitted to data of the mid-to-high  $T$  range were plotted as broken lines in Fig. 1a. The quadratic- $T$  dependence was applied to the low- $T$  data in the ‘over-doped’ region, where  $\rho(T)$  follows a  $T^2$  function, reminiscent of a correlated Fermi-liquid behaviour. The detailed fitting curves can be found in Extended Data Fig. 3. The temperatures at which experimental data deviate from the fittings are defined and plotted in Fig. 1c, as  $T_{\text{linear}}$  and  $T_{\text{FL}}$ . We note that for a universal ‘Planckian’ quasiparticle scattering scenario<sup>43</sup>, the hallmark ‘strange-metal’  $T$ -linear characteristic should dominate all temperatures free of superconducting correlations/fluctuations. Here,  $T_{\text{linear}}$  being markedly above  $T_c$  may relate to a low-temperature instability of magnetic interaction from local scattering centres, which will be the focus of the discussion later.

The next step is to further examine the role of Eu dopants across the phase diagram and their possible contribution to the (magneto-)transport properties. We first performed Hall effect measurements on a series of  $\text{SCE}_x$  samples. Fig. 2a shows a complete dataset of the Hall coefficient ( $R_H$ ) as a function of  $T$  for all samples with different  $x$ .  $R_H(T)$  were simply extracted from convenient linear fits to the Hall resistivity of the entire field range,  $\rho_{yx}(H)$ , at different temperatures. The behaviour of  $R_H(T)$  upon changing  $x$  reaffirms the hole doping effect induced by increasing  $\text{Eu}^{2+}$ : a sign change in  $R_H$  starts to emerge from being negative to positive around  $x \sim 0.22$ , which is right on top of the ‘dome’<sup>25,26,39</sup>; the sign-change temperature,  $T_{\text{cross}}$ , shows a non-trivial doping dependence. Initially,  $T_{\text{cross}}$  progressively shifts to higher temperatures with increasing doping, a trend analogous to previous observations in the  $\text{Ln}_{1-x}\text{Sr}_x\text{NiO}_2$  ( $\text{Ln} = \text{La}, \text{Pr}, \text{Nd}$ ) systems. However, when the doping level exceeds  $x = 0.3$ ,  $T_{\text{cross}}$  abruptly decreases, deviating from the expected monotonic increase<sup>25,26,39</sup>, as shown in Fig. 2b. This anomaly suggests a Fermi surface change occurring at higher doping concentrations, responsible for the change in  $R_H(T)$ . The  $\rho_{yx}(H)$  data of the representative samples are illustrated in Extended Data Fig. 4. We here choose a few to facilitate the discussion. For  $\text{SCE}_{0.22}$ ,  $R_H$  remains negative at all temperatures (above  $T_{c,\text{onset}}$ ) and  $\rho_{yx}(H)$  shows a typical linear feature; for  $\text{SCE}_{0.30}$ ,  $R_H$  changes sign from negative to positive at low temperatures (above  $T_{c,\text{onset}}$ ), while  $\rho_{yx}(H)$  maintains linear. These features are consistent with the doping dependence reported in the literature<sup>25,26,29,39</sup>. For the non-superconductive  $\text{SCE}_{0.50}$ , however, at  $T < 30$  K,  $\rho_{yx}(H)$  exhibits a salient non-linear feature at lower temperatures (for instance, at  $T = 2$  K). This behaviour, given the system being far outside the superconductivity state, suggests the presence of magnetism in the system, and that the itinerant electrons revealed from the Hall effect experiments are influenced by these magnetic moments, most likely rendered by the magnetic Eu ions.

Magnetic hysteresis measurements (magnetisation,  $M$ , versus  $H$ ) were performed at 3 K on three nickelate samples,  $\text{SCE}_{0.22}$ ,  $\text{SCE}_{0.34}$ , and  $\text{SCE}_{0.55}$ , as presented in Fig. 2c, e (with zoomed data in Fig. 2d, f). The  $\text{SCE}_{0.22}$  sample exhibits a characteristic paramagnetic response, confirming the absence of long-range magnetic order and close proximity to optimal  $T_c$  in this composition, in agreement with previous studies<sup>44,45</sup>. However, in the  $\text{SCE}_{0.34}$  and  $\text{SCE}_{0.55}$  samples, classic ferromagnetic magnetic hysteresis loops were observed, as shown in Fig. 2c-f. It is worth noting that the  $\text{SCE}_{0.34}$  sample is still within the superconducting dome, indicating

the coexistence of ferromagnetism and superconductivity and a spontaneous broken time-reversal symmetry in the sample. This is the first observation of (ferro-)magnetic ordering in nickelate superconductors, and of the coexistence of superconductivity and ferromagnetism in this system. Fig. 2e and f display the in-plane and out-of-plane magnetic hysteresis measurements of the  $\text{SCE}_{0.34}$  sample. From the coercive fields, although it is difficult to distinguish the direction of the magnetic easy axis, a weak anisotropy seems to suggest that the spontaneous magnetic moments are preferentially aligned out-of-plane. We further note that the observed magnetic moments seem to be anomalously enhanced by the Van Vleck paramagnetism related effect (see Extended Data Fig. 5 for  $M$ - $T$  data): For instance, in the  $\text{SCE}_{0.22}$  sample, the magnetic moments can reach up to  $400 \mu_B/\text{Eu}$  ( $\sim 8.75 \times 10^{-4}$  emu), while moments  $> 10 \mu_B/\text{Eu}$  are detected in the  $\text{SCE}_{0.34}$  and  $\text{SCE}_{0.55}$  samples; these values (far) surpass the theoretically expected value of  $7.94 \mu_B/\text{Eu}$ . Nevertheless, it is clear that an intrinsic ferromagnetism develops in the  $\text{SCE}_{0.34}$  and  $\text{SCE}_{0.55}$  samples at low temperatures. From these analyses, we correlate the aforementioned non-monotonic doping dependence of  $T_{\text{cross}}$  with the development of the ferromagnetic phase. As a result, the interplay between the ferromagnetic ordering and the superconducting state dominates the intriguing transport properties in this range of Eu concentration, as further evidenced below.

We now turn our focus to the ‘over-doped’ side of the phase diagram, where the strength of such magnetic interaction should be more prominent. Figure 3a shows the  $\rho(T)$  curves under a series of magnetic fields ( $\mu_0 H$ ) up to 14 T perpendicular to the film surface for a  $\text{SCE}_{0.32}$  sample. A typical field suppression of superconductivity until  $\sim 3$  T is visible, beyond which further increase of  $H$  leads to an enhancement of superconductivity as  $T_c$  becomes higher. This surprising field-enhanced superconductivity behaviour is potentially linked to the features of Eu, as in lower doping concentrations, no such enhancement was observed (for  $x < \sim 0.30$ ), as shown in Extended Data Fig. 6 and as discussed above, in this region, a ferromagnetic ordered state emerges, which may intertwine with the superconductivity under high fields.

The response to magnetic field of the ‘over-doped’  $\text{SCE}_x$  was further tested on another sample,  $\text{SCE}_{0.34}$ , with a thickness of  $\sim 20$  nm. As shown in Fig. 3b, the magneto-resistivity (MR),  $\rho(H)$ , exhibits a non-monotonic correspondence while  $\mu_0 H$  changes from 0 to 9 T, unambiguously illustrating the re-entrant behaviour. At  $T = 2$  K, a zero-resistance state was observed under  $\mu_0 H \geq \sim 6.23$  T. To interrogate the nature of the zero-resistance state and confirm the high-field re-entrant superconductivity, two-coil mutual inductance experiments were performed on this very sample. Despite a seemingly lower  $T_c$ , a clear diamagnetic response under 12 T can be observed (Fig. 3c), which, together with the signal at zero field, confirms the existence of two separated superconducting regimes. This superconducting-normal-superconducting transition, illustrated in Fig. 3c, largely resembles the re-entrant superconducting phase(s) that were discovered in heavy-fermion superconductors<sup>15–18,20–23</sup>, Chevrel phase compounds<sup>10,46</sup> and organic conductors<sup>11,14,47–50</sup>, which were ascribed to the interplay of the (local or ordered) magnetism and the (itinerant) superconductivity. Notably, spin-triplet superconducting pairing has been experimentally identified in heavy-fermion ferromagnetic superconductors such as URhGe and UCoGe, as well as in the high-field phase of  $\text{UTe}_2$ <sup>15,21,51</sup>. Our observation here raises the possibility of spin-triplet pairing in the high-field re-entrant phase of nickelate superconductors.

Attempting to fully unveil the behaviour of the re-entrant superconducting state, additional MR measurements were conducted under the ultrahigh magnetic fields provided by a high-field magnet facility (see Methods for details). Figure 3d displays the measured MR of a SCE<sub>0.32</sub> at different temperatures under a perpendicular field up to 35 T. A field-induced superconducting state is fully developed at high enough magnetic fields: the initial field applied mainly suppresses superconductivity with  $\rho(H)$  increasing from zero to finite values; above a critical field strength (3.23 T),  $\rho(H)$  drops again towards zero-resistance state and reaches a true zero around 13.04 T at  $T = 3$  K. This high-field zero-resistance state sustains above  $\sim 32$  T, displaying a remarkably robust re-entrant superconducting behaviour under high magnetic fields. Interestingly, the re-entrance is only clearly visible under a perpendicular magnetic field ( $H//c$ ), while almost absent for a parallel field ( $H\perp c$ , Fig. 2e). This is fundamentally different from the typical re-entrant superconductivity reported in example exotic 2D systems, where such phenomena were mainly present under the magnetic field applied in the sample plane<sup>11,52</sup>. We further measured the MR of a different sample, SCE<sub>0.36</sub>, down to 0.3 K under a magnetic field ( $H//c$ ) up to 45 T (Fig. 3f). Similarly, a pronounced re-entrant behaviour can be observed: at the lowest temperature,  $T = 0.3$  K, the ‘re-appeared’ zero-resistance state is barely suppressed even at 45 T, confirming the robustness of the newly found superconducting state.

This ‘hidden’ superconducting state lies in the ‘heavily doped’ side of the phase diagram ( $x > 0.30$ , as no clear ‘re-entrant’ behaviour was observed for SCE<sub>0.3</sub>, as shown in Extended Data Fig. 7), close to the boundary of the superconducting ‘dome’, where superconductivity starts to fade. One possible mechanism responsible for such an intriguing behaviour is the Jaccarino-Peter (J-P) compensation effect<sup>8</sup>, where in some cases, an internal exchange field ( $-H_{\text{ex}}$ ) imposed by the local magnetic ions (in this case, Eu), can act as a compensating field that opposes the external applied field ( $H_{\text{ext}}$ ). The mechanism is depicted in Fig. 4b. This could result in a re-entrant behaviour when the total magnetic field ( $H_{\text{tot}} = -H_{\text{ex}} + H_{\text{ext}}$ ) exerted upon the itinerant electrons is smaller than the upper critical field,  $H_{c2}$ . Despite the exact microscopic physical process for having a ‘negative’ exchange field may be unknown, the J-P effect can fairly account for the field-enhanced superconductivity, especially when the Eu ions with local magnetic moments are present<sup>10</sup>.

Within the framework of the J-P effect, the fact that the re-entrant behaviour is most obvious for  $H//c$  suggests that the moments of Eu are largely aligned out-of-plane, as the exchange field needs to be antiparallel to  $H_{\text{ext}}$ <sup>8</sup>. However, in the case of ‘over-doped’ SCE <sub>$x$</sub> , the re-entrance is present within a remarkably large range of the azimuthal angle of the magnetic field ( $\theta \sim 0 - 70^\circ$ ,  $\theta$  being the angle between sample surface normal and  $H$ ) in a rotation experiment as shown in Fig. 4a. This angle scale is much larger than that in other systems, such as UTe<sub>2</sub><sup>15,16,53</sup>, URhGe<sup>22,23</sup>, etc. These exotic features inform a more sophisticated picture at the microscopic level. A plausible scenario is rooted in the superconductivity being coexistent with an intertwined magnetic phase, as illustrated in Fig. 2c-f, facilitated by the magnetic Eu<sup>2+</sup>. In this context, the stabilisation of a possible ferromagnetic superconductivity at the phase boundary and/or near a (hidden) quantum critical point (QCP) can occur. The strong magnetic fluctuations (MF) caused by the destabilisation of the long-range magnetism can potentially enhance the superconducting pairing<sup>12,16,17,23</sup>; as a result, superconductivity can survive at and

on either side of the QCP, as shown in Fig. 4c. Our heavily doped IL system should involve both scenarios (J-P and MF mechanisms) at play.

## Discussion

The lattice compatibility of Eu in the A site of  $\text{SCE}_x$  largely enabled the unique materials platform for the investigation of a superconducting phase across a broad range of doping concentrations. This assists in overcoming the potential materials growth solubility limit, such as that encountered by Sr and Ca as dopants. The advantages of introducing Eu ions render the observation of a robust high-field superconducting state promoted by the magnetic interactions from an intriguing magnetic phase on the ‘over-doped’ side of the phase diagram, absent in other IL systems.

It is worth noting some interesting and unique aspects of this re-entrance behaviour. First, this is for the first time observed in a high- $T_c$  superconductor system, with the  $T_c$  of the  $\text{SCE}_x$  system much higher than other re-entrant systems<sup>15–23</sup>. Next, despite a generally large  $H_{c2}$  of the IL nickelate system, for certain Eu concentrations, the full superconducting state induced at high magnetic fields can be observed at a field as low as  $\sim 6$  T, making it easily accessible to be investigated. In addition, distinct from the usually observed re-entrant superconducting state under in-plane parallel field in other layer-structured materials systems<sup>11,14,47</sup>, in  $\text{SCE}_x$ , field-induced re-entrant superconductivity was observed at its strongest under perpendicular magnetic field with respect to the electron transport plane. A systematic angle-dependent re-entrant behaviour can be clearly seen with  $\theta$  in a remarkably wide range of  $\sim 0 - 70^\circ$  (Fig. 4a), larger than that observed in other systems<sup>11,14–16,22,23,47,53</sup>. Most importantly, the re-entrant behaviour vanishes when the magnetic field is applied in parallel to or closely aligned to the sample plane (e.g.  $\theta > \sim 70^\circ$  and approximates to  $90^\circ$ ). This is in stark contrast to the conventional re-entrant superconducting state, such as in two-dimensional superconductors, where the orbital de-pairing is quenched or suppressed and the Zeeman effect induced by in-plane magnetic field (typically aligned within a few degrees with respect to the direction of the local moments) is largely compensated, embodied by the J-P framework as discussed above<sup>8,14,47</sup>.

In fact, for a  $\text{SCE}_{0.32}$  sample measured at a higher temperature ( $T = 10$  K), except for a very narrow range of  $\theta$  precisely close to  $90^\circ$  (less than  $\pm 5^\circ$ ), all the  $\rho(H)$  curves show a clear sign of reduction at high fields (see Extended Data Fig. 7). This, together with the co-existence of a ferromagnetic phase (Fig. 2c-f) and superconductivity in the ‘over-doped’ regime (Fig. 4c), unambiguously suggests that spin fluctuations promoted by the in-plane component of the external field play an irreplaceable role in mediating the pairing in the second superconducting phase. This physical picture, analogous to the underlying mechanism of a magnetically mediated superconductivity for heavy fermion superconductors<sup>12,15–23</sup>, rather than a J-P scenario, invokes the tempting possibility of achieving a spin-triplet state, which warrants further exploration. One possible scenario for hosting such a time-reversal symmetry breaking triplet pairing state lies with Cooper pair spins pointing along  $c$ -axis and a primary interlayer pairing correlation: the  $H//c$  creates minimal orbital pairing breaking effects while  $H \perp c$  does not drive the re-entrant superconductivity.

The main observations and key ingredients relevant to superconductivity and the related magnetic phase in this intriguing IL nickelate system are then summarised into a rich phase diagram, illustrated in Fig. 4d, with key temperature scales labelled. From the phase diagram, we can clearly see the effect of an adjacent ferromagnetic phase, which emerges at the ‘over-doped’ side, on superconductivity, charge transport, quasi-particle scattering, etc. We note a few aspects as follows. First, the previously observed monotonic increase of  $T_{\text{cross}}$  for the sign change in  $R_H$ <sup>25,26,29,39</sup> and the hint for a ‘hidden’ QCP<sup>15,22,23</sup> are now disrupted by this co-existing ferromagnetic order, which underpins the nature of the re-entrant behaviour. The currently observed non-monotonic variation of  $T_{\text{cross}}$  may indicate another ‘hidden’ QCP under the superconducting ‘dome’, marking the boundary of the ferromagnetic phase, at an  $x$  value where  $T_{\text{cross}}$  is maximum. Furthermore, magnetic scatterings of electrons may dominate the low- $T$  quasi-particle transport below  $T_{\text{linear}}$ , when the  $T$ -dependence vanishes. Last and most importantly, all these phenomena suggest that the emergence of a ferromagnetic state, a possible Fermi surface change and the robust re-entrant superconductivity are strongly coupled.

In summary, we have unveiled a magnetic Eu-doping infinite-layer nickelate phase diagram in high-quality  $\text{Sm}_{0.95-x}\text{Ca}_{0.05}\text{Eu}_x\text{NiO}_2$  thin films with a remarkably wide range of Eu doping. On the over-doped side of the phase diagram, we observed a re-entrant superconducting state under ultrahigh magnetic fields up to 45 Tesla. This newly found superconducting phase is quite distinctive from the zero- (and low-) field superconductivity and points to a ferromagnetic superconducting state, which is evidenced by a triad of experimental evidence in one sample: (1) ferromagnetic  $M$ - $H$  hysteresis, (2) high-field zero resistance, and (3) high-field Meissner effect. These collective findings represent a paradigm shift, expanding the frontier of ferromagnetism-superconductivity research to the domain of higher-temperature correlated electrons.

## Methods

### Thin-film growth and preparation

Polycrystalline  $\text{Sm}_{0.95-x}\text{Ca}_{0.05}\text{Eu}_x\text{NiO}_y$  ceramic targets were synthesised by mixing stoichiometric ratios of  $\text{Sm}_2\text{O}_3$ ,  $\text{Eu}_2\text{O}_3$ ,  $\text{CaCO}_3$ , and  $\text{NiO}$  powders, followed by decarbonization at 1250 °C for 12 hours. After that, the targets were ground, re-pelletised and then sintered twice at 1300 °C and 1270 °C for 12 hours each.  $\text{Sm}_{0.95-x}\text{Ca}_{0.05}\text{Eu}_x\text{NiO}_3$  epitaxial films were deposited on  $5 \times 5 \text{ mm}^2$  LSAT (001) substrates via KrF excimer laser ( $\lambda = 248 \text{ nm}$ ) enabled pulsed laser deposition (PLD). Growth was performed at 600 °C under an oxygen partial pressure of 100 mTorr, with a laser fluence of 2.6 – 2.8 J/cm<sup>2</sup> and a repetition rate of 2 – 3 Hz. A ~2-nm-thick  $\text{SrTiO}_3$  capping layer was subsequently grown using a fluence of 0.6 J/cm<sup>2</sup>. Topotactic reduction was carried out *in situ* inside a vacuum chamber using  $\text{CaH}_2$  powders: The infinite-layer  $\text{Sm}_{0.95-x}\text{Ca}_{0.05}\text{Eu}_x\text{NiO}_2$  phase formation was tracked by real-time monitoring of the sample’s minimum resistance through a two-probe configuration. The process was conducted at a thermocouple-measured temperature range of ~270 – 310 °C for 0.5 - 1.5 hours.

### X-ray diffraction characterisation

The X-ray diffraction  $\theta - 2\theta$  symmetric scans of the films were obtained by a Rigaku SmartLab (9 kW) high-resolution X-ray diffractometer with the wavelength of the X-ray being 0.154 nm.

### **Lab-based transport measurements**

Wire connections for electrical transport measurements using the standard four-probe method were made with aluminium ultrasonic wire-bonded contacts. Resistivity and Hall-effect measurements were performed at temperatures down to 2 K and under magnetic fields up to 14 (or 9) T using Physical Properties Measurement Systems from Quantum Design Inc. Two-coil mutual inductance experiments were conducted with the driving and pickup coils aligned vertically above and below the thin film samples.

### **Magnetic measurements**

The magnetisation was measured using a superconducting quantum interference device (SQUID) magnetometer (MPMS-VSM, Quantum Design). Both zero-field-cooling (ZFC) and field-cooling (FC) modes were employed to measure the magnetisation between 3 K and 380 K under a magnetic field of 100 Oe. Isothermal magnetisation curves were recorded in the applied magnetic field range of -3 T to +3 T at different temperatures for  $M(H)$  measurements.

### **High-magnetic-field measurements**

High-magnetic-field magnetoresistance measurements were performed at the Chinese High Magnetic Field Laboratory (CHMFL) in Hefei. The experiments utilized a 35 T water-cooled magnet and a 45.2 T hybrid magnet<sup>54</sup>, which are equipped with a  $^3\text{He}$  cryostat. Magnetoresistance was measured using SR830 lock-in amplifiers with a built-in a.c. current source.

### **X-ray absorption spectroscopy measurements**

The soft X-ray absorption spectroscopy (XAS) measurements at the Eu- $M$  edge for the prepared samples were conducted at room temperature using total electron yield (TEY) mode on the BL08U1A soft X-ray spectro-microscopy beamline at the Shanghai Synchrotron Radiation Facility (SSRF).

## References

1. Keimer, B., Kivelson, S. A., Norman, M. R., Uchida, S. & Zaanen, J. From quantum matter to high-temperature superconductivity in copper oxides. *Nature* **518**, 179–186 (2015).
2. Dagotto, E. Correlated electrons in high-temperature superconductors. *Rev. Mod. Phys.* **66**, 763–840 (1994).
3. Taillefer, L. Scattering and pairing in cuprate superconductors. *Annu. Rev. Condens. Matter Phys.* **1**, 51–70 (2010).
4. Han, T. *et al.* Signatures of chiral superconductivity in rhombohedral graphene. *Nature* **643**, 654–661 (2025).
5. Kallin, C. & Berlinsky, J. Chiral superconductors. *Rep. Prog. Phys.* **79**, 054502 (2016).
6. Sato, M. & Ando, Y. Topological superconductors: a review. *Rep. Prog. Phys.* **80**, 076501 (2017).
7. Qi, X.-L. & Zhang, S.-C. Topological insulators and superconductors. *Rev. Mod. Phys.* **83**, 1057–1110 (2011).
8. Jaccarino, V. & Peter, M. Ultra-high-field superconductivity. *Phys. Rev. Lett.* **9**, 290 (1962).
9. Fischer, O. H. Properties of high-field superconductors containing localized magnetic moments. *Helv. Phys. Acta* (1972).
10. Meul, H. W. Observation of magnetic-field-induced superconductivity. *Phys. Rev. Lett.* **53**, 497–500 (1984).
11. Uji, S. *et al.* Magnetic-field-induced superconductivity in a two-dimensional organic conductor. *Nature* **410**, 908–910 (2001).
12. Aoki, D. *et al.* Unconventional superconductivity in heavy fermion  $\text{UTe}_2$ . *J. Phys. Soc. Jpn.* **88**, 043702 (2019).
13. Lebed, A. G. Quantum limit in a magnetic field for triplet superconductivity in a quasi-one-dimensional conductor. *Phys. Rev. B* **90**, (2014).
14. Konoike, T. Magnetic-field-induced superconductivity in the antiferromagnetic organic superconductor  $\kappa\text{-(BETS)}_2\text{FeBr}_4$ . *Phys. Rev. B* **70**, (2004).
15. Ran, S. *et al.* Extreme magnetic field-boosted superconductivity. *Nat. Phys.* **15**, 1250–1254 (2019).
16. Frank, C. E. *et al.* Orphan high field superconductivity in non-superconducting uranium ditelluride. *Nat Commun* **15**, 3378 (2024).
17. Helm, T. *et al.* Field-induced compensation of magnetic exchange as the possible origin of reentrant superconductivity in  $\text{UTe}_2$ . *Nat Commun* **15**, 37 (2024).
18. Niu, Q. Fermi-surface instability in the heavy-fermion superconductor  $\text{UTe}_2$ . *Phys. Rev. Lett.* **124**, (2020).
19. Saxena, S. S. *et al.* Superconductivity on the border of itinerant-electron ferromagnetism in  $\text{UGe}_2$ . *Nature* **406**, 587–592 (2000).
20. Aoki, D., Ishida, K. & Flouquet, J. Review of U-based ferromagnetic superconductors: comparison between  $\text{UGe}_2$ ,  $\text{URhGe}$ , and  $\text{UCoGe}$ . *J. Phys. Soc. Jpn.* **88**, 022001 (2019).
21. Aoki, D. *et al.* Coexistence of superconductivity and ferromagnetism in  $\text{URhGe}$ . *Nature* **413**, 613–616 (2001).
22. Lévy, F., Sheikin, I., Grenier, B. & Huxley, A. D. Magnetic field-induced superconductivity in the ferromagnet  $\text{URhGe}$ . *Science* **309**, 1343–1346 (2005).

23. Lévy, F., Sheikin, I. & Huxley, A. Acute enhancement of the upper critical field for superconductivity approaching a quantum critical point in URhGe. *Nat. Phys.* **3**, 460–463 (2007).
24. Li, D. *et al.* Superconductivity in an infinite-layer nickelate. *Nature* **572**, 624–627 (2019).
25. Li, D. Superconducting dome in Nd<sub>1-x</sub>Sr<sub>x</sub>NiO<sub>2</sub> infinite layer films. *Phys. Rev. Lett.* **125**, (2020).
26. Zeng, S. Phase diagram and superconducting dome of infinite-layer Nd<sub>1-x</sub>Sr<sub>x</sub>NiO<sub>2</sub> thin films. *Phys. Rev. Lett.* **125**, (2020).
27. Zeng, S. *et al.* Superconductivity in infinite-layer nickelate La<sub>1-x</sub>Ca<sub>x</sub>NiO<sub>2</sub> thin films. *Sci. Adv.* **8**, eabl9927 (2022).
28. Osada, M. *et al.* A Superconducting praseodymium nickelate with infinite layer structure. *Nano Lett.* **20**, 5735–5740 (2020).
29. Osada, M. Phase diagram of infinite layer praseodymium nickelate Pr<sub>1-x</sub>Sr<sub>x</sub>NiO<sub>2</sub> thin films. *Phys. Rev. Mater.* **4**, (2020).
30. Osada, M. *et al.* Nickelate superconductivity without rare-earth magnetism: (La,Sr)NiO<sub>2</sub>. *Adv. Mater.* **33**, 2104083 (2021).
31. Wei, W., Vu, D., Zhang, Z., Walker, F. J. & Ahn, C. H. Superconducting Nd<sub>1-x</sub>Eu<sub>x</sub>NiO<sub>2</sub> thin films using in situ synthesis. *Sci. Adv.* **9**, eadh3327 (2023).
32. Chow, S. L. E., Luo, Z. & Ariando, A. Bulk superconductivity near 40 K in hole-doped SmNiO<sub>2</sub> at ambient pressure. *Nature* **642**, 58–63 (2025).
33. Yang, M. *et al.* Enhanced superconductivity in co-doped infinite-layer samarium nickelate thin films. Preprint at <https://doi.org/10.48550/arXiv.2503.18346> (2025).
34. Hepting, M. *et al.* Electronic structure of the parent compound of superconducting infinite-layer nickelates. *Nat. Mater.* **19**, 381–385 (2020).
35. Wang, B. Y., Lee, K. & Goodge, B. H. Experimental progress in superconducting nickelates. *Annu. Rev. Condens. Matter Phys.* **15**, 305–324 (2024).
36. Chen, Z. *et al.* Electronic structure of superconducting nickelates probed by resonant photoemission spectroscopy. *Matter* **5**, 1806–1815 (2022).
37. Ding, X. *et al.* Cuprate-like electronic structures in infinite-layer nickelates with substantial hole dopings. *Nat. Sci. Rev.* **11**, nwae194 (2024).
38. Sun, W. *et al.* Electronic structure of superconducting infinite-layer lanthanum nickelates. *Sci. Adv.* **11**, eadr5116 (2025).
39. Lee, K. *et al.* Linear-in-temperature resistivity for optimally superconducting (Nd,Sr)NiO<sub>2</sub>. *Nature* **619**, 288–292 (2023).
40. Richter, J. H. *et al.* Electronic structure of EuN: growth, spectroscopy, and theory. *Phys. Rev. B* **84**, 235120 (2011).
41. Tcakaev, A. *et al.* Incipient antiferromagnetism in the Eu-doped topological insulator Bi<sub>2</sub>Te<sub>3</sub>. *Phys. Rev. B* **102**, 184401 (2020).
42. Negusse, E. *et al.* Effect of electrode and EuO thickness on EuO-electrode interface in tunneling spin filter. *J. Appl. Phys.* **99**, 08E507 (2006).
43. Hartnoll, S. A. *Colloquium*: Planckian dissipation in metals. *Rev. Mod. Phys.* **94**, (2022).
44. Fowlie, J. *et al.* Intrinsic magnetism in superconducting infinite-layer nickelates. *Nat. Phys.* **18**, 1043–1047 (2022).
45. Lu, H. *et al.* Magnetic excitations in infinite-layer nickelates. *Science* **373**, 213–216 (2021).



46. Burlet, P. *et al.* Magnetism and superconductivity in the Chevrel phase  $\text{HoMo}_6\text{S}_8$ . *Physica B* **215**, 127–133 (1995).
47. Uji, S. & S. Brooks, J. Magnetic-field-induced superconductivity in organic conductors. *J. Phys. Soc. Jpn.* **75**, 051014 (2006).
48. Balicas, L. Superconductivity in an organic insulator at very high magnetic fields. *Phys. Rev. Lett.* **87**, (2001).
49. Uji, S., Kobayashi, H., Balicas, L. & Brooks, J. s. Superconductivity in an organic conductor stabilized by a high magnetic field. *Adv. Mater.* **14**, 243–245 (2002).
50. Uji, S. *et al.* Global phase diagram of the magnetic field-induced organic superconductors  $\lambda\text{-(BETS)}_2\text{Fe}_x\text{Ga}_{1-x}\text{Cl}_2$ . *J. Phys. Soc. Jpn.* **72**, 369–373 (2003).
51. Ran, S. *et al.* Nearly ferromagnetic spin-triplet superconductivity. *Science* **365**, 684–687 (2019).
52. Cao, Y., Park, J. M., Watanabe, K., Taniguchi, T. & Jarillo-Herrero, P. Pauli-limit violation and re-entrant superconductivity in moiré graphene. *Nature* **595**, 526–531 (2021).
53. Knebel, G. *et al.* Field-reentrant superconductivity close to a metamagnetic transition in the heavy-fermion superconductor  $\text{UTe}_2$ . *J. Phys. Soc. Jpn.* **88**, 063707 (2019).
54. Fang, Z. *et al.* Design of a 42 T resistive magnet at the CHMFL. *IEEE Trans. Appl. Supercond.* **34**, 1–4 (2024).

## Figures

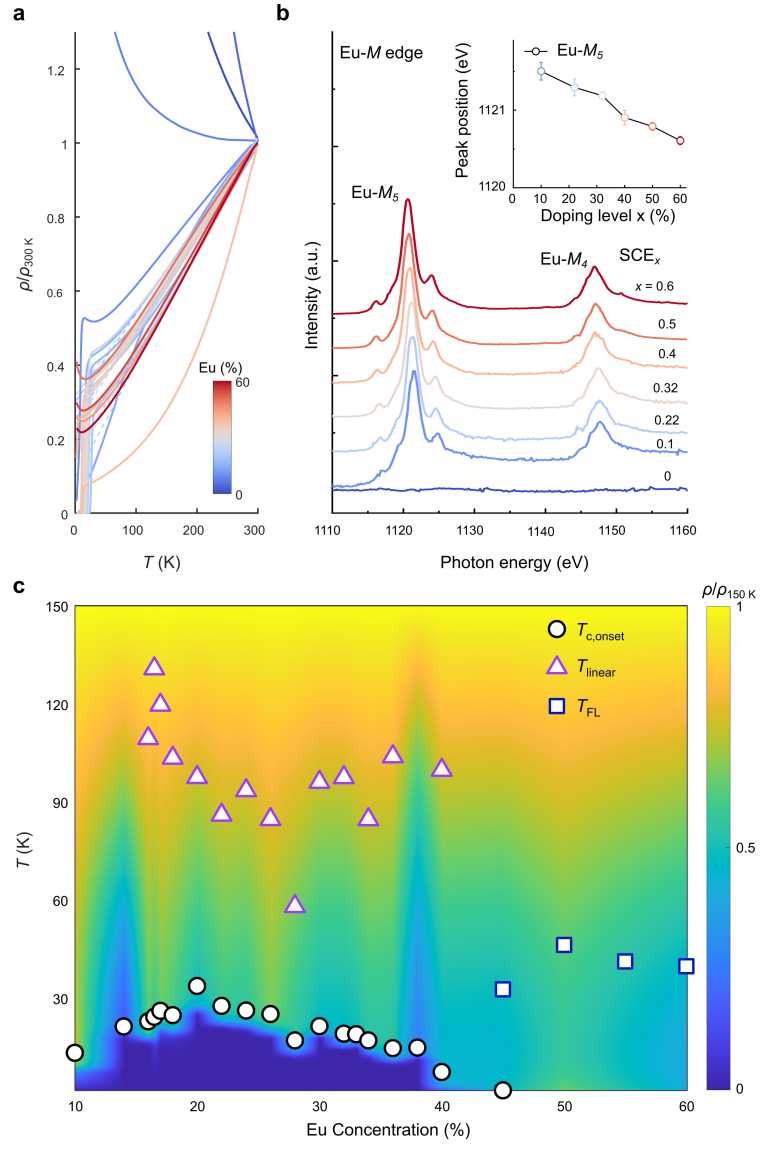


**Fig. 1 | Eu doping dependent resistivity, electronic state and phase diagram of  $\text{Sm}_{0.95-x}\text{Ca}_{0.05}\text{Eu}_x\text{NiO}_2$  ( $\text{SCE}_x$ ).** **a**, The normalised resistivity ( $\rho(T)/\rho(300\text{ K})$ ) as a function of temperature for a set of representative samples with different  $x$  ( $0 \leq x \leq 0.60$ ). **b**, X-ray absorption spectroscopy of  $\text{SCE}_x$  ( $x = 0, 0.1, 0.22, 0.32, 0.4, 0.5, 0.6$ ) showing the  $M$  edge of Eu. Each curve was normalised with reference to the Eu-M<sub>5</sub> peak intensity. Inset: The peak positions of the Eu-M<sub>5</sub> edge extracted from the main panel of **b** plotted against  $x$ . A clear decrease in the energy values can be observed as  $x$  increases, showcasing a doping effect. **c**, A contour plot with the colour code representing the normalised resistivity ( $\rho(T)/\rho(150\text{ K})$ ) values as a function of  $x$ , showing the superconducting phase.  $T_{\text{c,onset}}$ , the onset of superconductivity, defined as the temperature below which the  $\rho$  data start to drop below a linear extrapolation of the normal-state  $\rho(T)$ ;  $T_{\text{linear}}$ , the characteristic temperature below which the data deviate from the linear fits to  $\rho(T)$ ;  $T_{\text{FL}}$ , the characteristic temperature above which the data deviate from the  $T^2$  fits to  $\rho(T)$ .

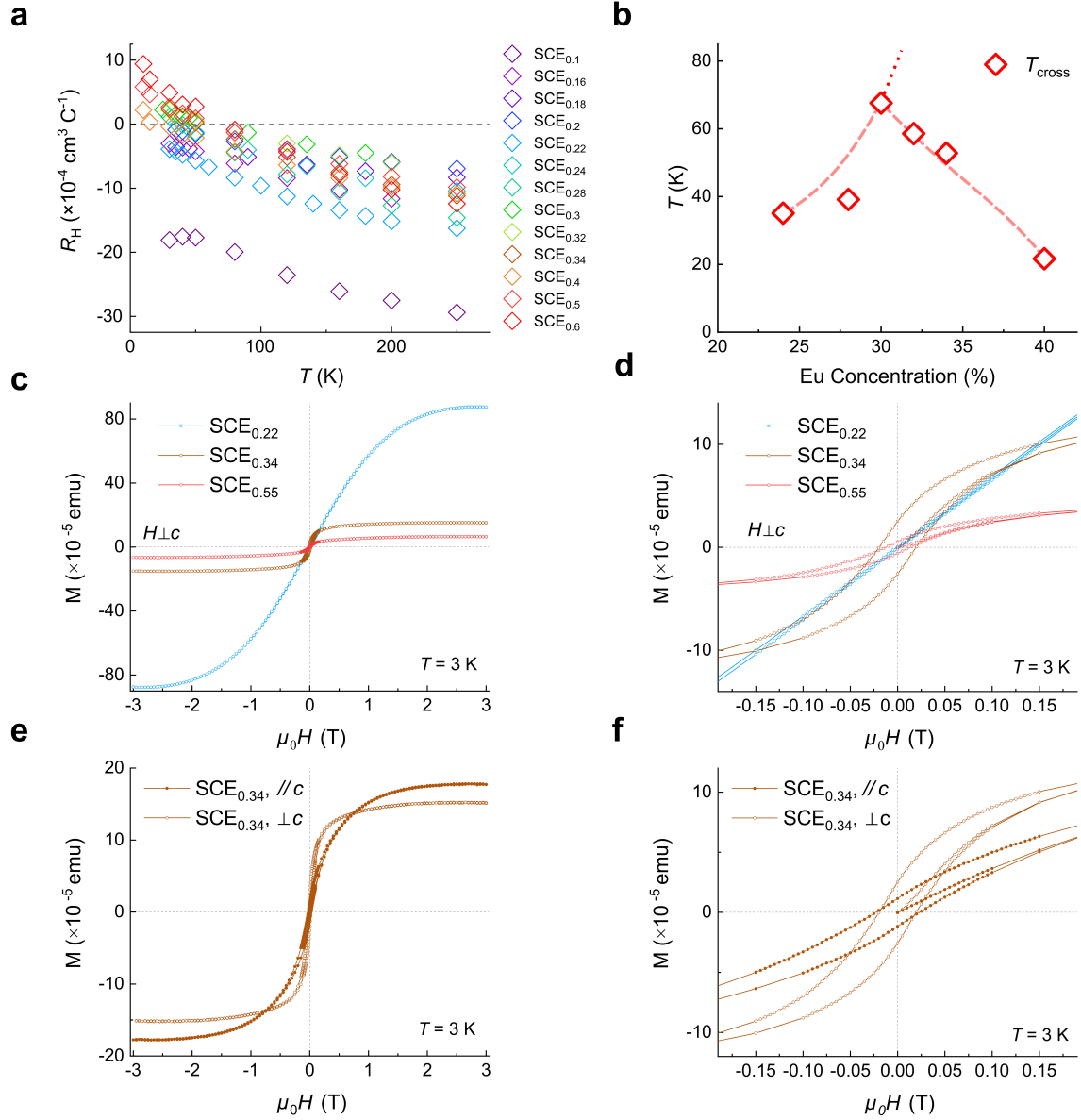


**Fig. 2 | Hall effect measurements and characterisations on ferromagnetism.** **a**, Hall coefficient,  $R_H$ , as a function of temperature for samples with varying Eu doping concentrations. Note that there is a sign change in  $R_H$  when the Eu concentration  $x$  is more than 0.24. **b**, The sign-change temperature,  $T_{\text{cross}}$ , as a function of Eu concentration. The dashed line is a guide to the eye. The dotted line is a typical extrapolation of the doping dependence of  $T_{\text{cross}}$  as shown for previously reported IL nickelates. **c** and **d**, The magnetisation as a function of magnetic field,  $M(H)$ , measured for  $H \perp c$  for three samples (SCE<sub>0.22</sub>, SCE<sub>0.34</sub>, SCE<sub>0.55</sub>) at 3 K both at full scale and in zoomed view: clear hysteresis loops can be observed for SCE<sub>0.34</sub> and SCE<sub>0.55</sub>. **e** and **f**, full-scale and zoomed  $M(H)$  curves for SCE<sub>0.34</sub> measured along both  $H \parallel c$  and  $H \perp c$  at 3 K.

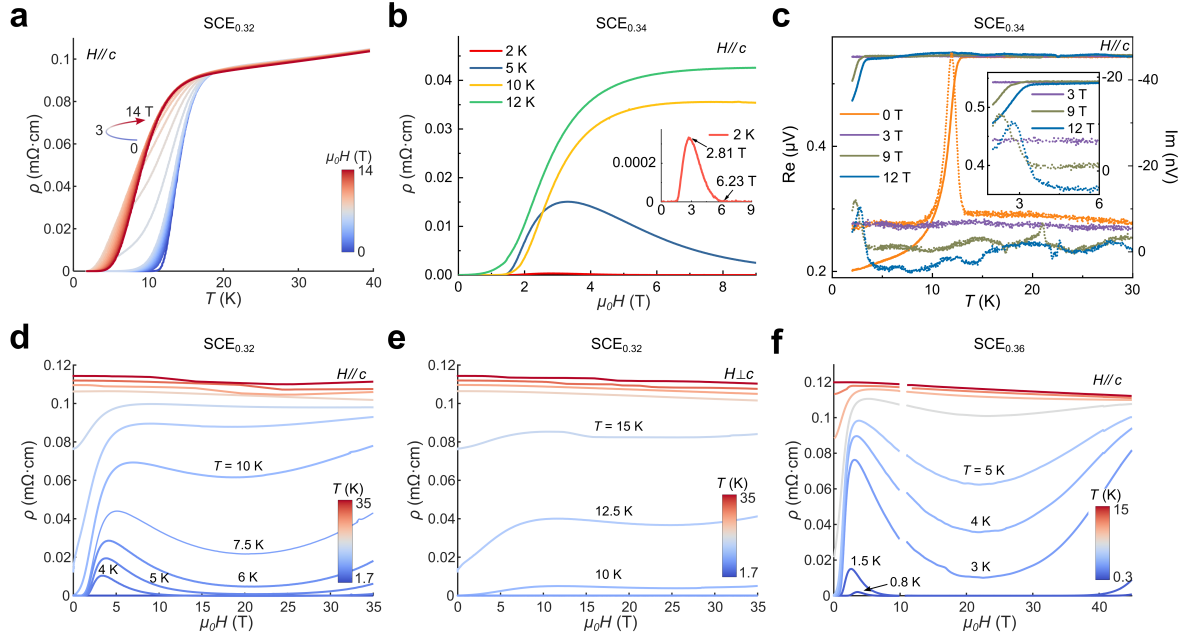


**Fig. 3 | Magnetotransport of ‘over-doped’  $\text{SCE}_x$  samples illustrating the re-entrant superconducting state.** **a**,  $\rho(T)$  curves of a  $\text{SCE}_{0.32}$  sample under magnetic fields:  $T_c$  initially decreases and subsequently increases with magnetic field. **b**,  $\rho(H)$  of a  $\text{SCE}_{0.34}$  sample ( $\sim 20$  nm).  $\rho$  drops back to zero above 6.23 T at 2 K (Inset shows a zoomed view of  $\rho(H)$  at 2 K). **c**, Mutual inductance measurement under various magnetic fields ( $H//c$ ). The real ( $\Delta\text{Re}$ ) and imaginary ( $\Delta\text{Im}$ ) signals show typical diamagnetic responses for  $\mu_0H = 0$  T, which are absent for  $\mu_0H = 3$  T. At  $\mu_0H = 9$  T and 12 T, a drop in  $\Delta\text{Re}$  and a peak in  $\Delta\text{Im}$  can be clearly seen, indicating the diamagnetic screening effect due to a re-entrant superconductivity. Inset shows a zoomed view of the data for  $\mu_0H = 3, 9, 12$  T. **d** and **e** The  $\rho(H)$  curves up to 35 T, along  $H//c$  and  $H\perp c$ , at different  $T$  for a  $\text{SCE}_{0.32}$  sample. **f**, The  $\rho(H)$  curves up to 45 T with  $H//c$  at different  $T$  for a  $\text{SCE}_{0.36}$  sample. For **d** and **f**, a clear re-entrant behaviour can be observed with an out-of-plane field ( $H//c$ ) for  $\text{SCE}_{0.32}$  and  $\text{SCE}_{0.36}$ , while no obvious re-entrant behaviour is observed with an in-plane field ( $H\perp c$ ) as shown in **e**.

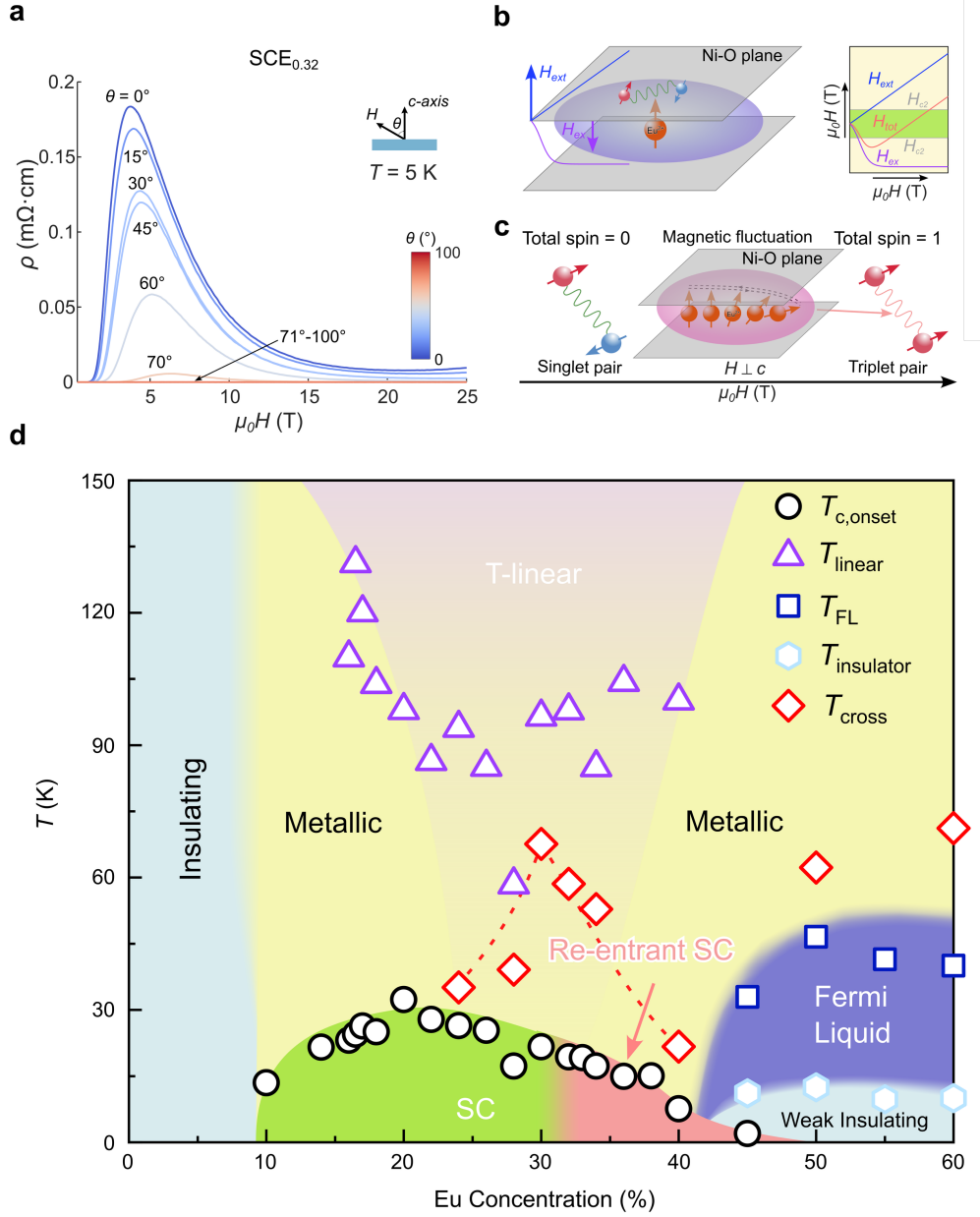


**Fig. 4 | Mechanisms for the high-field superconducting state and the phase diagram of  $\text{Sm}_{0.95-x}\text{Ca}_{0.05}\text{Eu}_x\text{NiO}_2$ .** **a**,  $\rho(H)$  up to 25 T with different  $\theta$  angles for a  $\text{SCE}_{0.32}$  sample at 5 K.  $\theta$  is the angle between  $H$  and the sample surface normal.  $\theta$  for  $\rho(H)$  with the highest peak was set as 0° for calibration. **b**, The Jaccarino-Peter (J-P) compensation effect. Left panel sketches the schematic of the generation of an internal exchange field ( $H_{\text{ex}}$ , purple) with an applied external field ( $H_{\text{ext}}$ , blue); right panel illustrates the mechanism of the J-P effect:  $H_{\text{ex}}$  counteracts  $H_{\text{ext}}$ , leading to a re-entrant superconductivity when the total internal field ( $H_{\text{tot}}$ , red) is less than  $H_{c2}$ . **c**, Ferromagnetic superconductivity stabilises near a quantum critical point (QCP): magnetic fluctuations—arising from the destabilisation of long-range magnetic order—enhance superconducting pairing. In this case, superconductivity can persist at the QCP and on both sides of it. **d**, The superconducting phase diagram of  $\text{Sm}_{0.95-x}\text{Ca}_{0.05}\text{Eu}_x\text{NiO}_2$  with all key characteristic temperatures discussed in the main text. The broken line is a guide to the eye.

## **Acknowledgements**

We acknowledge the funding support from the National Natural Science Foundation of China (12174325) and a Guangdong Basic and Applied Basic Research Grant (2023A1515011352). The research was supported by research grants from the Research Grants Council (RGC) of the Hong Kong Special Administrative Region, China, under Early Career Scheme, General Research Fund and ANR-RGC Joint Research Scheme (CityU 21301221, CityU 11309622, CityU 11300923 and A-CityU102/23). Part of the work utilised the equipment support through a Collaborative Research Equipment Grant from RGC (C1018-22E). Part of this work was supported by the National Key R&D Program of China (2024YFA1408101 and 2022YFA1403101), the Natural Science Foundation of China (92265112, 12374455 and 52388201), the Guangdong Provincial Quantum Science Strategic Initiative (GDZX2401004 and GDZX2201001), the Shenzhen Science and Technology Program (KQTD20240729102026004), and the Shenzhen Municipal Funding Co-Construction Program Project (SZZX2301004 and SZZX2401001). The high-magnetic-field work was supported by the National Key R&D Program of China (2023YFA1607701) and the National Natural Science Foundation of China (51627901). Z.W. acknowledges the support of U.S. Department of Energy, Basic Energy Sciences Grant No. DE-FG02-99ER45747. We thank the staff members of the SMA and WM5 System at the Steady High Magnetic Field Facility, Chinese Academy of Sciences, for providing technical support and assistance in data collection.

## **Author contributions**

M.Y., J.T., X.W. contributed equally to this work. M.Y., H.W., Z.C. and D.L. conceived the research project. M.Y., J.T. and W.X. grew the samples. W.X. and M.Y. synthesised polycrystalline targets. H.W., X.W., Z.P. and W.X. performed the in-situ reduction experiments. H.W., X.W., W.X., M.Y., J.T. and Z.P. performed transport measurements. H.W. conducted the mutual inductance measurements. M.Y. conducted the magnetic measurements with the help of H.H. and S.H. H.W., M.Y., and H.H. conducted the high field measurements with the help of G.K., C.X., L.P., and Q.L. M.Y. and J.X. conducted the XAS measurements. Z.W. provided theoretical interpretations. Q.X., Z.C., and D.L. acquired funding support. M.Y., J.T., H.W., Z.C., and D.L. wrote the manuscript with contributions from all authors.

## **Competing interests**

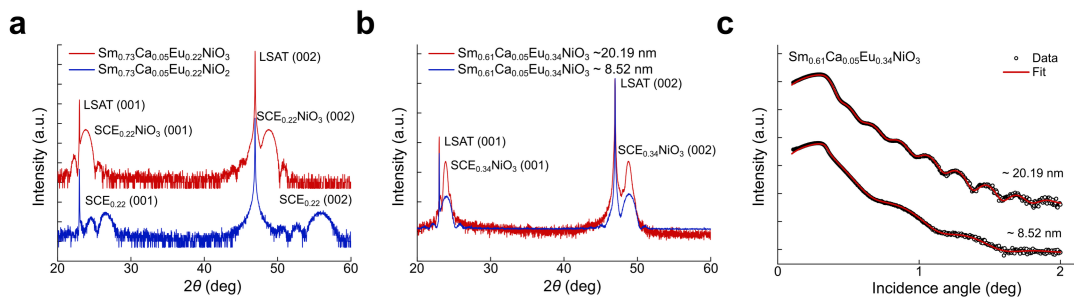
The authors declare that they have no competing interests.

## **Additional information**

Supplementary information: The online version contains supplementary materials available at (to be filled).

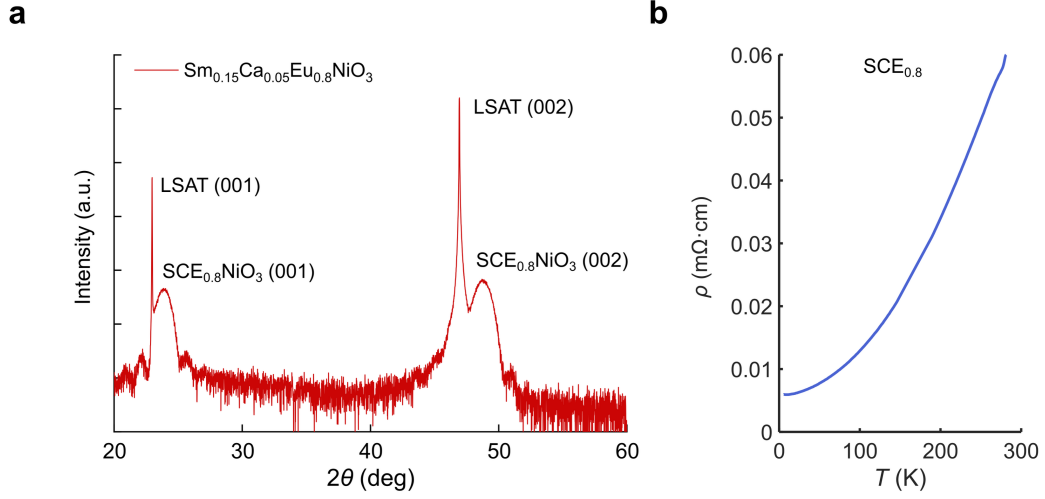
Correspondence and requests for materials should be addressed to Heng Wang, Zhuoyu Chen or Danfeng Li

## Extended Data Figures

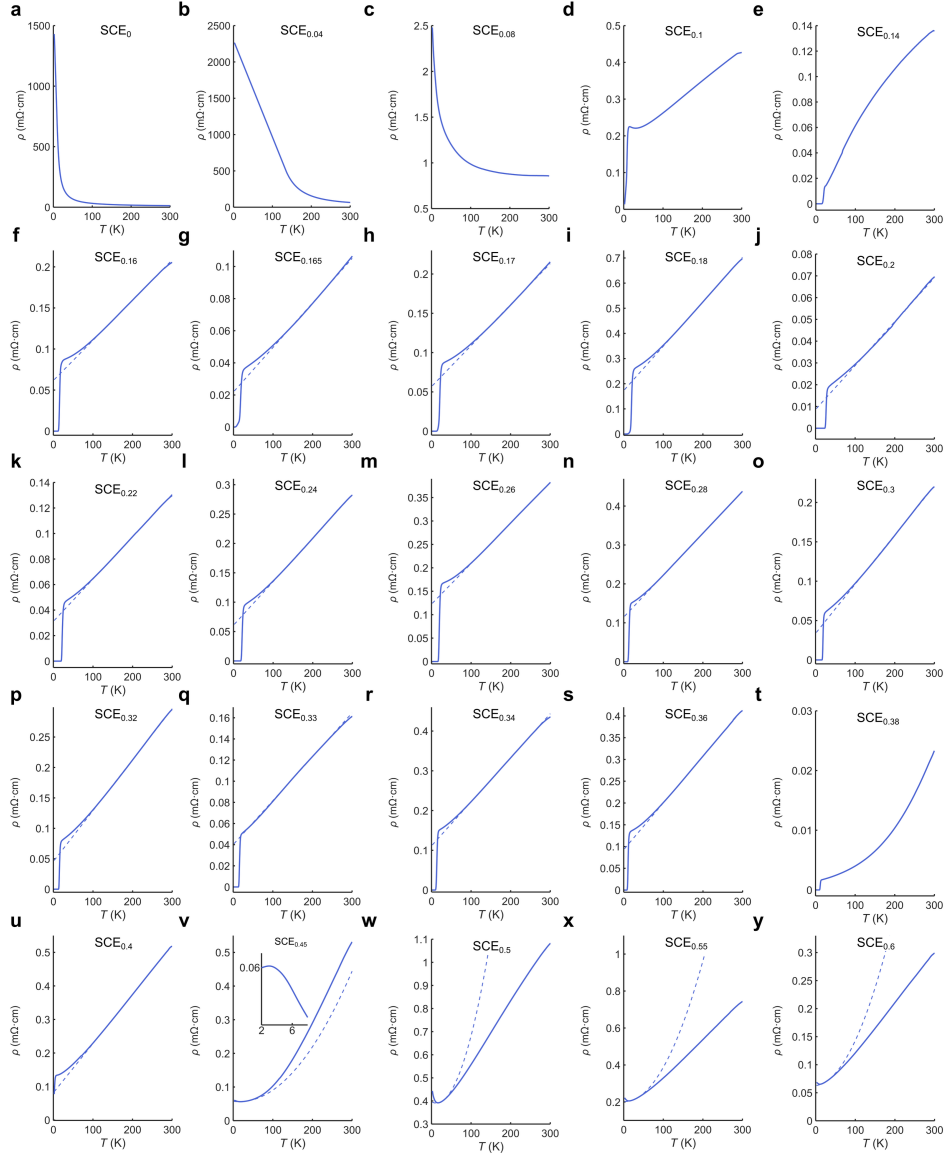


**Extended Data Fig. 1 | The structural characterisations of the samples.** a and b, X-ray diffraction (XRD)  $\theta$ - $2\theta$  symmetric patterns of  $\text{Sm}_{0.73}\text{Ca}_{0.05}\text{Eu}_{0.22}\text{NiO}_{3(2)}$  and  $\text{Sm}_{0.61}\text{Ca}_{0.05}\text{Eu}_{0.34}\text{NiO}_3$  thin films. The presence of prominent (001) film peaks with finite-size oscillations and their peak positions all suggest good film crystallinity across wide ranges of doping and film thickness. c, X-ray reflectivity (XRR) patterns for  $\text{Sm}_{0.61}\text{Ca}_{0.05}\text{Eu}_{0.34}\text{NiO}_3$  thin films with thicknesses of  $\sim 8.52$  nm and  $\sim 20.19$  nm. In experiments, the infinite-layer phase samples with varying doping levels all have a thickness of  $\sim 8$  nm. The sample  $\text{SCE}_{0.34}$  used for the mutual inductance two-coil measurements has a thickness of  $\sim 20$  nm.

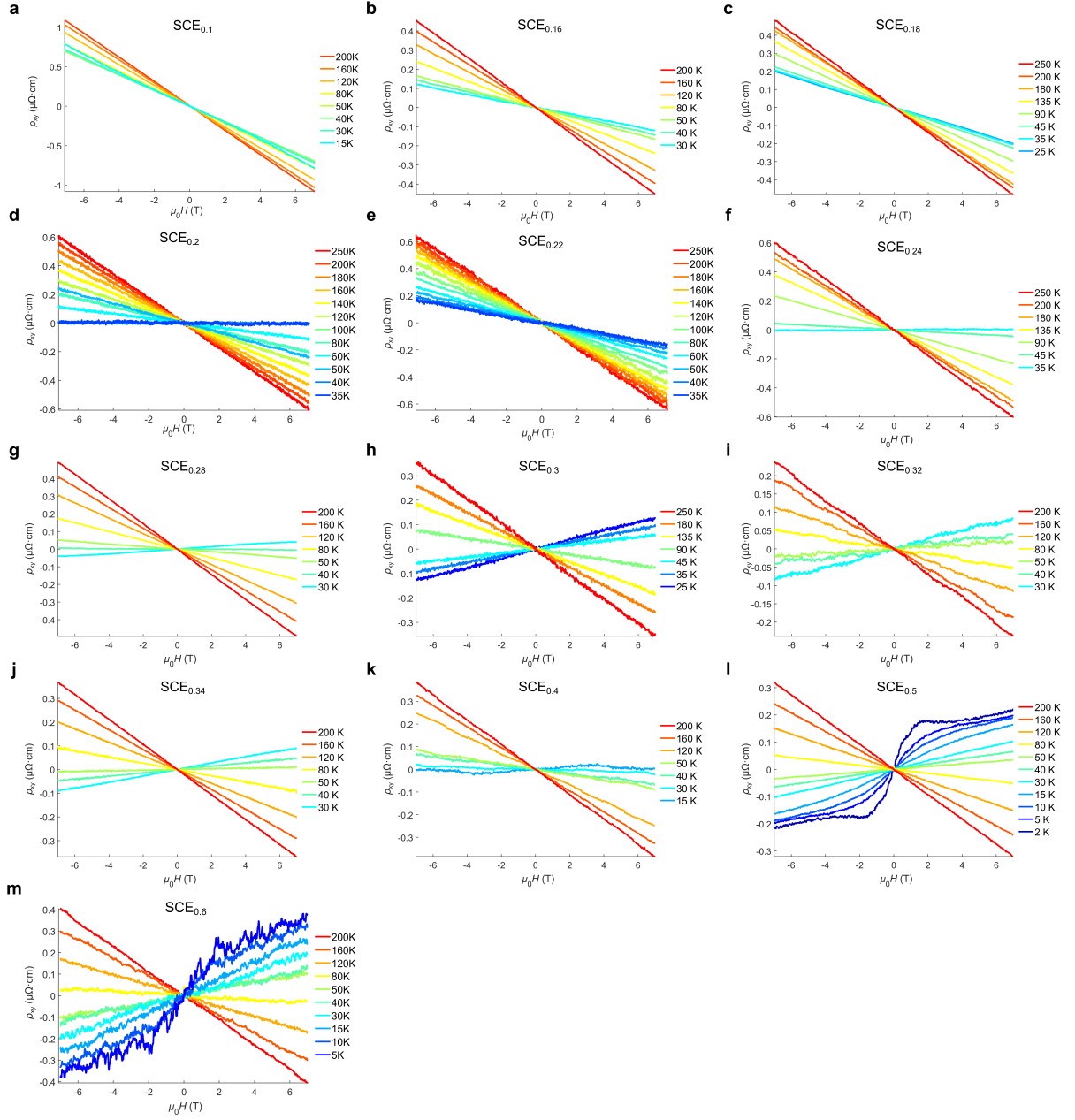




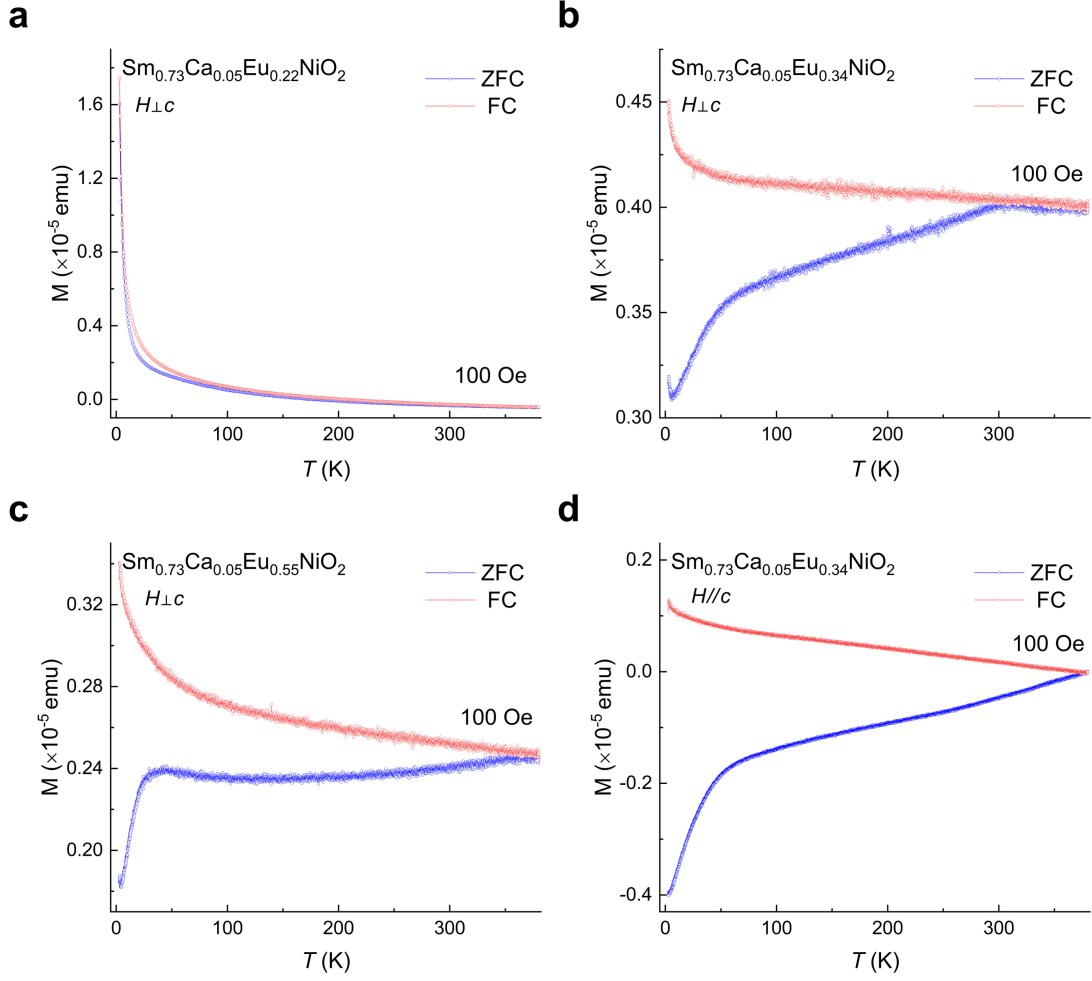
**Extended Data Fig. 2 | Heavily doped sample.** a, X-ray diffraction (XRD)  $\theta$ - $2\theta$  symmetric scan of a  $\text{Sm}_{0.15}\text{Ca}_{0.05}\text{Eu}_{0.8}\text{NiO}_3$  sample. The data indicates that excellent film crystallinity is achieved across a wide range of Eu concentration up to an extremely high doping level. b,  $\rho(T)$  curve of a  $\text{Sm}_{0.15}\text{Ca}_{0.05}\text{Eu}_{0.8}\text{NiO}_2$  ( $\text{SCE}_{0.8}$ ) sample. The  $\text{SCE}_{0.8}$  sample exhibits a metallic behaviour across the entire temperature range.



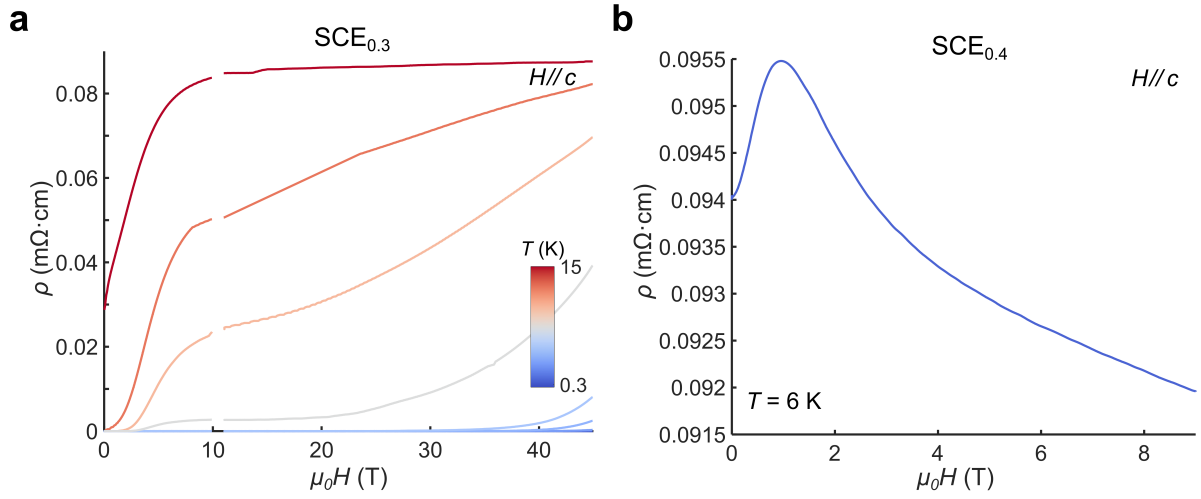
**Extended Data Fig. 3 | Individual  $\rho(T)$  curves of  $\text{Sm}_{0.95-x}\text{Ca}_{0.05}\text{Eu}_x\text{NiO}_2$  ( $\text{SCE}_x$ ) across all doping levels.** The dashed lines are the linear (or quadratic) fits to the data. The inset of Panel v is the zoom-in curve at low temperatures, showing a ‘transition’ feature near  $T = 2.3$  K.



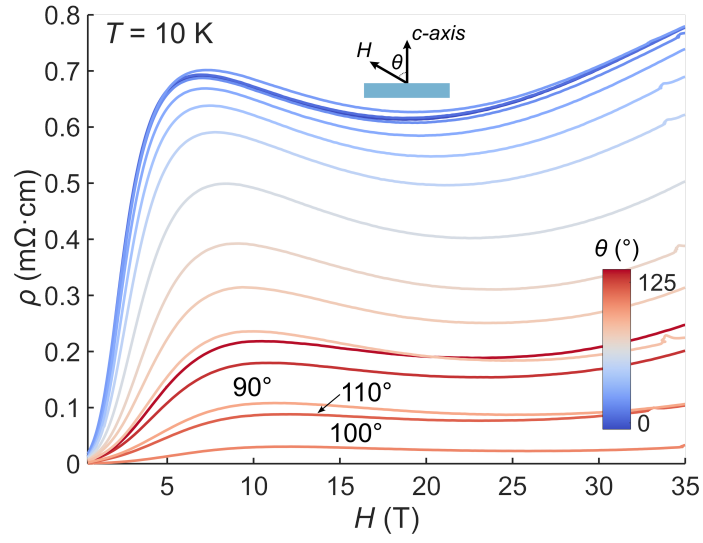
**Extended Data Fig. 4 | Hall resistivity of  $\text{SCE}_x$  samples across different regimes.** No sign change in Hall coefficient ( $R_H$ , slope of  $\rho_{yx}(H)$ ) for  $x$  lower than 0.24; Sign change in  $R_H$  for  $x$  over 0.24; Nonlinear Hall resistivity at low temperature for  $x = 0.4, 0.5$  and  $0.6$ .



**Extended Data Fig. 5 | Magnetisation as a function of temperature for  $\text{SCE}_x$  ( $x = 0.22$ ,  $0.34$  and  $0.55$ ) samples.** a, b and c, The in-plane magnetisation as a function of temperature ( $M$ - $T$ ) for samples with Eu doping levels of 0.22, 0.34, and 0.55, respectively, for both zero-field cooling and field-cooling under a field of 100 Oe. d, The out-of-plane  $M$ - $T$  curves for  $\text{SCE}_{0.34}$ .



**Extended Data Fig. 6 |  $\rho(H)$  up to 45 T at different temperatures for a  $\text{SCE}_{0.3}$  sample and  $\rho(H)$  of a  $\text{SCE}_{0.4}$  sample at 6 K under out-of-plane fields.** Here, the  $\rho(H)$  for  $\text{SCE}_{0.3}$  shows no re-entrant behaviour up to 45 T, clearly demarcating a lower limit of the re-entrant regime. The  $\rho(H)$  of  $\text{SCE}_{0.4}$  shows a sign of reduction with the increase of fields, indicating that the upper limit of the re-entrant regime is larger than  $x = 0.4$ .



**Extended Data Fig. 7 |  $\rho(H)$  up to 35 T with different  $\theta$  angles for a  $\text{SCE}_{0.32}$  sample at 10 K.**  $\theta$  is the angle between  $H$  and the sample surface normal. The  $\rho(H)$  curves show a sign of reduction at high fields.